Simultaneous generation of oxygen vacancies on ultrathin BiOBr nanosheets during visible-light-driven CO_2 photoreduction evoked superior activity and long-term stability

Xin Ying Kong[a], Boon-Junn Ng[a], Kok Hong Tan[b], Xiaofang Chen[c], Huanting Wang[c], Abdul Rahman Mohamed[d], Siang-Piao Chai[a,*]

[a] Multidisciplinary Platform of Advanced Engineering, Chemical Engineering Discipline, School of Engineering, Monash University, Jalan Lagoon Selatan, Bandar Sunway, 47500, Selangor, Malaysia
[b] Mechanical Engineering Discipline, School of Engineering, Monash University, Jalan Lagoon Selatan, Bandar Sunway, 47500, Selangor, Malaysia
[c] Department of Chemical Engineering, Monash University, Clayton, Victoria, 3800, Australia
[d] Low Carbon Economy (LCE) Group, School of Chemical Engineering, Universiti Sains Malaysia, Engineering Campus, Seri Ampangan, 14300, Nibong Tebal, Pulau Pinang, Malaysia

ARTICLE INFO

ABSTRACT

Under the tremendous pressure of imminent energy crisis and anthropogenic climate change, photocatalytic conversion of abandoned CO_2 into energy-rich hydrocarbon fuels is highly desirable. However, this solar-to-fuel conversion is unavoidably suppressed by the fast recombination of electron-hole pairs and lack of stability of photocatalysts. To overcome this, we have developed ultrathin BiOBr nanosheets (BOB-NS) with primarily exposed {001} facets. The {001} facets of BOB-NS are comprised of high density O atoms, which are linked to the neighbouring Bi atoms *via* weak Bi−O bonds with long bond length and low bond energy. After visible-light-driven CO_2 photoreduction over BOB-NS, we found that the Bi−O bonds were broken and oxygen vacancy (OV) defects formed on the sample surface. The presence of these OVs was proven to be beneficial for photoactivities as photoinduced electrons were effectively trapped at the OV sites and recombination of charge carriers were inhibited. Generally, the free O atoms from dissociation of CO_2 would reoxidize the sample surface, thereby deteriorating the performance of photocatalysts. In contrast, we demonstrated in this study that the OV sites on BOB-NS could be simultaneously regenerated and refreshed as the reactions proceeded, leading to a sustainable activity and long-term stability for CO_2 photoreduction.

1. Introduction

Photocatalytic conversion of carbon dioxide (CO_2) into energy-rich hydrocarbon fuels provides the vista of addressing environmental issues and imminent energy crisis concurrently [1–3]. Yet so far, the realization of this technology is still a mirage as the efficiency of CO_2 reduction is often thwarted by the undesirable electron-hole pair recombination and lack of long-term stability of photocatalysts. In this regard, more extensive studies on enhancing the photoactivity and stability of semiconductors are of paramount significance in order to develop an efficient and practical photocatalytic system.

The recent flourishes in defect engineering of semiconductor photocatalysts are provoking a surge of interest in developing two-dimensional (2D) nanosheets with synthetically induced surface defects. Numerous recent publications have been focusing on oxygen vacancy (OV) defects on metal oxides, where these OVs were attested to significantly alter the optical and electronic properties of photocatalysts [4–7]. The presence of OVs could result in the formation of defect states between conduction band (CB) and valence band (VB) of semiconductor photocatalysts, which act as excellent electron sink to effectively trap photoinduced electrons and inhibiting the recombination of charge carriers [8]. In addition, surface OVs with abundant localized electrons have been reported as the active sites for adsorption and activation of reactants, where surface reactions could be initiated once the reactants adsorbed on the OV sites [9–11]. In the context of CO_2 photoreduction, this is highly desirable as the reactions are difficult to take place due to the thermodynamically stable of CO_2 molecules. With the merits of surface OV defects, it has been proposed that the introduction of surface OVs on metal oxide semiconductors could be a feasible strategy for boosting the performance of photocatalysts for CO_2 reduction.

To affirm this hypothesis, bismuth oxybromide (BiOBr) was selected as the model semiconductor metal oxide among all the potential candidates. As a main group of V-VI-VII ternary oxide with unique layered crystal structure, BiOBr has been reported as a promising photocatalyst owing to its remarkable properties of inexpensiveness, non-toxicity, naturally abundance, suitable bandgap energy (E_g ~ 2.8 eV) and appropriate energy band positions [12–14]. In the atomic level, the positively charged $[Bi_2O_2]^{2+}$ slabs are interleaved by two slabs of bromine atoms, resulting in the formation of self-built internal static electric field perpendicular to each layer [15]. This inherent internal static electric field is favourable as it facilitates the separation of photoinduced electron-hole pairs. Similar to other 2D nanomaterials, BiOBr also possesses fascinating facet-dependent photocatalytic activities, where the reaction rate and production yield are highly affected by the exposed facets of the crystal. For BiOBr, the {001} facets have been known as the most active facet for photocatalytic reduction-related activities [16]. In this regard, the fabrication of BiOBr with ultrathin nanosheet structures and primarily exposed {001} facets is highly desirable in order to explore its full potential. Coincidentally, the {001} facets of BiOBr are terminated with a large density of oxygen atoms, providing high possibility for the formation of OV defects [17]. To date, there are a few studies have reported on the fabrication of bismuth-based nanomaterials with OV defects, including the use of strong reducing agent such as ethylene glycol or glycerol, post-treatments of the samples in H_2-rich environment or under high-powered UV light irradiation to break the Bi−O bonds [18–22]. However, these approaches still suffer from several drawbacks. For instance, the presence of ethylene glycol or glycerol in the synthesis result in the structure transformation of BiOBr, where 2D nanosheets are assembled into 3D microspheres. The post-treatments of sample are often complicated and require large amount of energy inputs, curtailing the practical applications of these approaches. Under these circumstances, the development of a cost-effective and efficient approach for spatial location engineering of OVs is of paramount importance.

Herein, we present an extremely facile one-step hydrothermal approach for the synthesis of ultrathin BiOBr nanosheets with highly exposed {001} facets, where the surface OVs were easily formed during the visible-light-driven CO_2 photoreduction experiments. To the best of our knowledge, this is the first study reporting on the simultaneous generation of OVs on BiOBr nanosheets during the CO_2 photocatalytic reduction, without involving any reducing agent or post-treatment for the formation of OVs. More importantly, the as-developed ultrathin BiOBr nanosheets were found to have long-lasting photoactivities as these OVs could be simply refreshed as the reactions proceeded, providing sustainable active sites for CO_2 reduction. We believe that the findings from the current study will deliver some new and imperative insights into the development and design of surface defect-engineered photocatalysts with robust performance and long-term stability for a myriad of applications.

2. Materials and methods

2.1. Chemical reagents

All the chemical reagents were utilized as received without any further purification. Bismuth (III) nitrate pentahydrate, $Bi(NO_3)_3 \cdot 5H_2O$ (≥98.0%), potassium bromide, KBr (≥99.0%), sodium hydroxide, NaOH (≥98.5%), nitric acid, HNO_3 (≥90.0%) and Degussa P25 (≥99.5%) were purchased from Sigma Aldrich. Ethanol, C_2H_5OH (96.0%) was procured from Friendemann Schmidt Chemical. Deionized water (resistivity ≥ 18 MΩ cm) was used throughout the experiment.

2.2. Preparation of photocatalysts

Ultrathin BiOBr nanosheets with dominant exposed {001} facets were synthesized *via* a facile one-pot hydrothermal approach. Typically,

5 mmol $Bi(NO_3)_3 \cdot 5H_2O$ was slowly added into 80 mL of deionized water containing a stoichiometric amount of KBr. The pH of the solution was adjusted to 6 using 2.0 M NaOH aqueous solution, and the resulting dispersion was stirred for 1 h at room temperature. Then, the mixture solution was transferred into a Teflon-lined stainless steel autoclave, which was heated at 160 °C for 12 h with continuous stirring. After completion of reaction, the solution was cooled naturally to room temperature. Subsequently, the resultant precipitate was collected and washed repeatedly with ethanol and deionized water to remove residual ions. Finally, the obtained powder was dried in an air oven at 60 °C for 12 h, and denoted as BOB-NS. For comparison, BiOBr nanoplates (BOB-NP) was synthesized followed the same procedures as that of BOB-NS, except that the pH of the solution was adjusted to 1 using 1.0 M HNO_3 during the synthesis.

2.3. Characterization

The sample structures and morphologies were examined by a Hitachi SU 8010 field emission scanning electron microscopy (FESEM). Transmission electron microscopy (TEM), high-resolution TEM (HRTEM) images and selected-area electron microscopy (SAED) patterns were taken by a TECNAI G2 F20 transmission electron microscope operating at 200 kV. The specimen for TEM imaging was prepared by depositing a drop of sample suspension in ethanol onto a carbon-coated copper grid. The crystallographic phase composition of the samples was determined by a Bruker D8 Discover X-ray diffractometer using Ni-filtered Cu Kα radiation (λ = 1.5406 Å) at a scan rate of 0.02 s^{-1}. For the analysis, the accelerating voltage and applied current were set at 40 kV and 40 mA, respectively. Raman spectra was attained by a Horiba LabRAM HR Evolution spectrometer with a laser excitation at λ = 514 nm. The X-ray photoelectron spectroscopy (XPS) survey and narrow scan spectra were recorded by a PHI Quantera II, Ulvac-PHI, INC., equipped with an Al K$_\alpha$ X-ray source ($h\nu$ = 1486.6 eV) at 10 mA and 15 kV, and analyzed under ultra-vacuum environment of 2.4×10^{-6} Pa. All the spectra obtained were charged corrected by means of adventitious carbon signal (C 1s peak) at 284.6 eV. The ultraviolet–visible (UV–vis) absorption spectra of the samples were revealed by a UV–vis spectrophotometer (Agilent, Cary 100) equipped with an integrated sphere. The bandgap energies were determined from the Kubelka-Munk (KM) function, $F(R)$ and the extrapolation of the Tauc plot $[F(R) \cdot h\nu]^{1/2}$ to the abscissa of photon energy, $h\nu$.

2.4. Electrochemical analysis

The transient photocurrent responses and electrochemical impedance spectroscopy (EIS) Nyquist plots and of the as-fabricated photocatalysts were obtained by an electrochemical workstation (CHI 6005E) in a conventional three-electrode quartz cell. The working electrode was obtained by drop-casting the samples in ethanol suspension (5 mg/mL) onto a fluorine-doped tin oxide (FTO) glass slide with an electroactive area fixed at 1.0 cm^2, while Pt served as counter electrode and Ag/AgCl saturated with 3 M KCl employed as reference electrode. All three electrodes were immersed in the electrolyte (0.5 M Na_2SO_4) during the analysis. A 500 W Xenon arc lamp (CHF-XM-500W) equipped with an UV cut-off filter (to provide visible light with λ > 400 nm) was employed as the exciting visible light source.

2.5. Evaluation of photocatalytic CO_2 reduction activities

The photoreduction of CO_2 into CH_4 experiments were performed in a custom-made, continuous gas flow reactor. Typically, the as-developed photocatalysts were uniformly coated on glass rods where the mass loading of the photocatalysts was fixed at 30 mg to ensure a fair comparison between the samples. Then, the coated glass rods were inserted into quartz columns and high purity CO_2 (99.999%) were bubble through H_2O to generate a mixture of CO_2/H_2O as reactant gas.

The reactant gas was directed to the quartz columns to allow intimate contact with the photocatalysts. Prior to light irradiation, the reactant gas was bubbled at a flow rate of 50 mL/min for 30 min to evacuate air from the system and to allow the reactant gas to completely adsorb on the photocatalyst surface. Henceforth, the flow rate of reactant gas was reduced to 5 mL/min and the photocatalysts were irradiated by a 500 W Xenon arc lamp (CHF-XM-500W) equipped with an UV cut-off filter (remove $\lambda < 400$ nm) to provide visible light source. The product gas was taken at every 1 h interval and the components were analyzed and quantified by gas chromatography (Agilent 7820 A) equipped with flame ionized detector (FID) and thermal conductivity detector (TCD). The experiment was conducted at atmospheric pressure and room temperature, and the set-up was kept in a black box to avoid surrounding light interference (Fig. S1 in the supplementary information). The CH_4 yield from the photocatalytic CO_2 reduction experiment was quantified using Eq. (1).

$$CH_4 \text{ yield } (\mu mol\, g^{-1} h^{-1})$$
$$= \frac{(C_{final, CH4} - C_{initial, CH4}) \times \text{volumetric flow rate of product gas}}{\text{Mass of photocatalyst used (g)}} \quad (1)$$

3. Results and discussion

The structural features and surface morphologies of the as-synthesized ultrathin BiOBr nanosheets (BOB-NS) were examined by electron microscopy. From the FESEM images, BOB-NS was observed to be in flaky nanostructure with the lateral size in the range of 80–500 nm and thickness of *ca.* 10 nm (Fig. 1A and inset) (See Fig. S2 in the supplementary information for the FESEM images of pristine BiOBr nanoplates). TEM image further affirmed the ultrathin nature of the BOB-NS, where nearly transparent appearance was observed (Fig. 1B). The HRTEM image showed clear lattice fringes with an interplanar lattice

spacing of 0.278 nm at 90°, which corresponded to the (110) atomic plane of BiOBr perpendicular to the (001) atomic plane (Fig. 1B inset). This suggests that the as-fabricated BOB-NS predominantly exposed {001} facets, as illustrated by the tetragonal crystal orientation in Fig. 1B inset. To confirm this, SAED spots of BOB-NS were analyzed (Fig. 1C). The corresponding SAED pattern revealed the single-crystalline characteristic of BOB-NS. The angle between the adjacent spots were measured to be 45°, which is in good agreement with the theoretical angle between (110) and (200) planes. This set of SAED spots could be readily indexed to the [001] zone axis of tetragonal BiOBr, and it can be confirmed that the BOB-NS was enclosed with dominant {001} facets. To further establish the tetragonal nanostructure of BOB-NS, XRD analysis was performed. As shown in Fig. 1D, the peaks located at 10.9°, 22.0°, 25.3°, 31.8°, 32.3°, 33.3°, 39.4°, 46.3°, 50.8° and 57.3° could be indexed to the (001), (002), (011), (012), (110), (003), (112), (020), (014) and (212) crystal planes of pure tetragonal phase of BiOBr (JCPDS card no. 73–2061, space group: P4/*nmm*, unit cell parameters: $a = 3.915$ Å, $b = 3.915$ Å and $c = 8.076$ Å). These intense and sharp peaks exhibited by BOB-NS implied that the sample is well-crystallized. Besides, no foreign peaks were detected, suggesting that the sample is of high-purity. It is worth noting that BOB-NS exhibited a much intense diffraction peak at (110) compared to the peaks at (001), (002) and (003), suggesting that the growth of BOB-NS is more favorable along the [110] orientation that is perpendicular to the *c* axis, giving rise to the formation of ultrathin slabs [22–24]. This finding further affirmed our successful synthesis of BOB-NS with ultrathin nanostructures and primarily exposed {001} facets.

To have better understanding on the atomic arrangement of different facets of BiOBr, BiOBr crystal was modelled through the visualization for electronic and structural analysis (VESTA). Scheme 1A shows the tetragonal matlockite-type structure of BiOBr, which is characterized by alternating $[Bi_2O_2]^{2+}$ slab and two slabs of Br atoms.
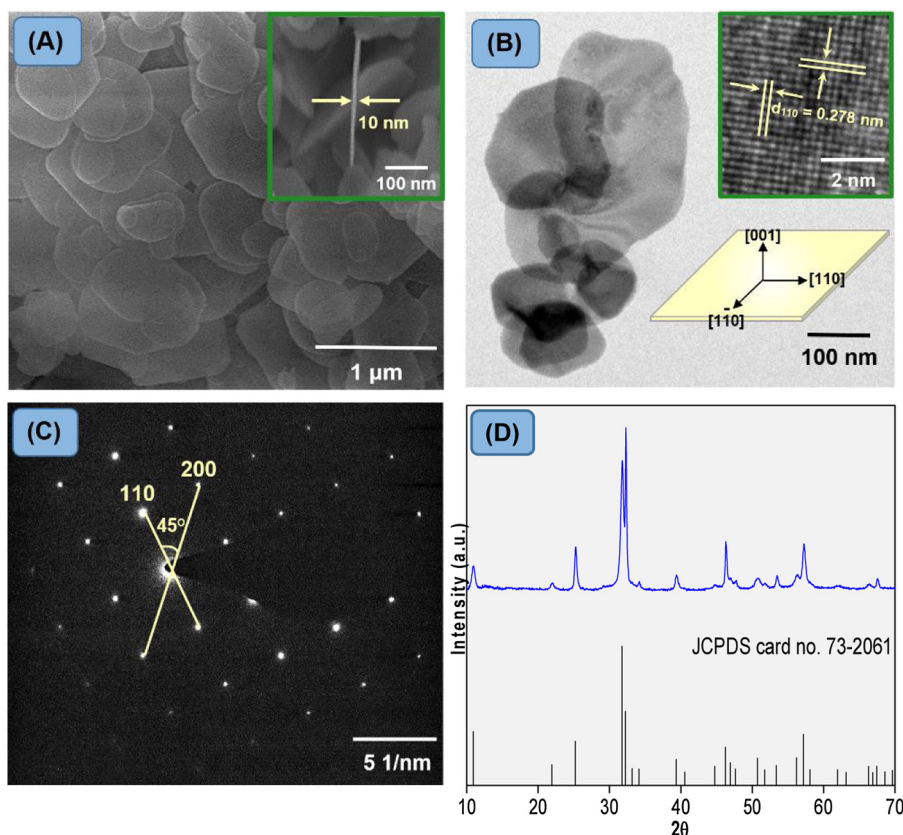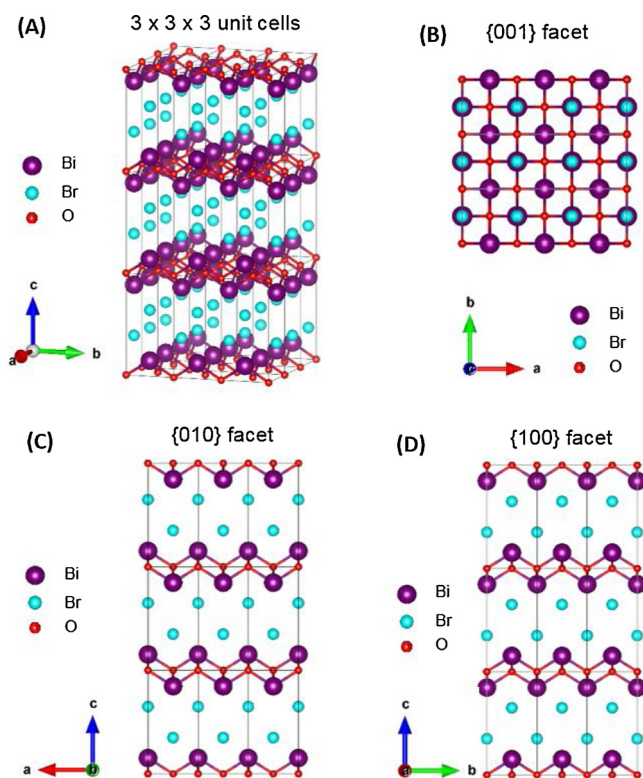

Fig. 1. (A) FESEM image (inset displays the thickness of the sample), (B) TEM image (insets display the HRTEM image and schematic illustration of tetragonal crystal orientation), (C) SAED pattern and (D) XRD pattern of BOB-NS.

Scheme 1. Schematic illustrations of BiOBr crystals, showing (A) 3D projection, (B) {001} facet, (C) {010} facet and (D) {100} facet simulated by VESTA.

The $[Bi_2O_2]^{2+}$ slabs are formed by the strong covalent bonding whereas the Br atoms are held by the weak Van der Waals interaction, resulting in the formation of self-built internal electric field. The {001}, {010} and {100} facets of BiOBr are illustrated in Scheme 1B–D, respectively. In comparison to {010} and {100} facets, the {001} facets were observed to possess high density of Bi and O atoms. Since the Bi–O bonds are with long bond length and low bond energy, it is easier for the OVs to form on {001} facets to that of {010} and {100} facets [13]. Therefore, it is anticipated that the BOB-NS with high exposure of {001} facets is favourable for the formation of OV defects, leading it to exhibit superior photocatalytic activities.

To verify this, the as-synthesized BOB-NS was tested for photocatalytic CO_2 reduction under visible light irradiation ($\lambda > 400$ nm). The experiments were performed in a custom-made gas phase reactor, where the experimental conditions were kept at room temperature and atmospheric pressure to mimic the natural environment. A series of control experiments was carried out, including: i) no light irradiation, ii) no CO_2 (under N_2/H_2O flow) and iii) no H_2O (under dry CO_2 flow). Under all these conditions, negligible amount of reaction product was generated from these control experiments (Fig. S3), which affirmed that the carbon-containing product formation was triggered by solely photoreduction of CO_2 and the possibility of the occurrence of photolysis or decomposition of organic residues on the photocatalyst was excluded. In addition, light source and CO_2/H_2O reactant feeds are indispensable for the photocatalytic reactions to take place.

Fig. 2 shows the production rate of CH_4 ($\mu mol\, g^{-1}\, h^{-1}$) from photocatalytic reduction of CO_2 under visible light irradiation. The production yield of BOB-NS was observed to increase over the reaction time, achieving a maximum rate of $2.15\, \mu mol\, g^{-1}\, h^{-1}$, which was 3.3 folds higher compared to the pristine BiOBr nanoplates (BOB-NP). The superior performance of BOB-NS is primarily caused by the synergistic effects of its ultrathin structures with predominantly exposed {001} facets. As aforementioned, the {001} facet of BiOBr is the most reactive facet for photocatalytic reduction activities and the dominant {001}

exposed facets of BOB-NS provide more active sites for the CO_2 reduction. In addition, the reducing of the sample thickness to an ultrathin-nanoscale could dramatically enhance its photocatalytic performance, which was also demonstrated in our previous work [25]. This endows the ultrafast transfer of photoinduced electron-hole pairs from the interior to the surface of photocatalysts, which in turn facilitate the separation of charge carriers, inhibiting the occurrence of electron-hole pair bulk recombination. Interestingly, the ultrathin BOB-NS was observed to turn from yellowish-white to darkish-grey in colour after photocatalytic CO_2 reduction experiment, where no such significant colour change was observed for BOB-NP and Degussa P25. This phenomenon suggests the possible simultaneous generation of OVs in ultrathin BOB-NS during the CO_2 photoreduction under solely visible light irradiation. As we know, the dramatic colour change of the metal oxide semiconductors is an indication of OV defects formation as the presence of these OV-induced defect state allows sub-bands excitation of photogenerated electrons [26,27]. For the BOB-NS, the decrease of sample thickness to ultrathin nanoscale led to a large exposure of interior atoms on the photocatalyst surface, which significantly altered its surface atomic structure, including coordination number, bond length and possible formation of atom disorder. In the light of this, surface structure disoder such as OV defects could be easily created on the ultrathin BOB-NS sample.

To ascertain our hypothesis, XPS analysis was performed over fresh BOB-NS and spent BOB-NS after visible light irradiation (BOB-NS-VLT). Based on the XPS survey spectra, Bi, O and Br were observed in both BOB-NS and BOB-NS-VLT, which are in good agreement with the chemical compositions of the samples (Fig. 3A). As disclosed by the high resolution Bi 4f spectra (Fig. 3B), BOB-NS exhibited two peaks at 159.4 and 164.7 eV, representing the Bi $4f_{7/2}$ and Bi $4f_{5/2}$ spin-orbital splitting photoelectrons in the Bi^{3+} chemical state, respectively. In comparison, a 0.1 eV shift to higher binding energy was demonstrated by BOB-NS-VLT and two additional small peaks at 161.0 and 166.0 eV were formed. These observations of peak shifting and existence of additional peaks could be classically ascribed to the presence of $Bi^{(3-x)+}$ chemical state, owing to the existence of OV defects. Further evidence of the presence of OVs on BOB-NS-VLT was provided by the high resolution O 1s spectra (Fig. 3C). The asymmetric nature of the peaks revealed the co-existence of low binding energy component (LBEC) and high binding energy component (HBEC) [28]. The LBEC at 530.2 eV could be attributed to the lattice oxygen (O_{latt}) species whereas the HBEC at 532.0 eV corresponded to the adsorbed oxygen (O_{ads}) such as surface hydroxylation and adsorbed H_2O. As widely accepted, the density of OVs could be reflected by the intensity of HBEC [29]. For BOB-NS, the ratio of LBEC to HBEC was 6.31 whereas the ratio was decreased to 5.77 for BOB-NS-VLT, which further attested the presence of OVs on BOB-NS-VLT. As could be seen from Fig. 3D, the high resolution Br 3d spectrum of BOB-NS could be deconvoluted into two peaks at 68.5 and 69.5 eV, which could be ascribed to the $3d_{5/2}$ and $3d_{3/2}$ of Br– chemical state, respectively. For the case of BOB-NS-VLT, a 0.2 eV shift to higher binding energy was observed, implying a change in the electron density due to the formation of OVs.

Further evidence of the formation of OVs on BOB-NS-VLT was reflected by Raman spectroscopy. All the characteristic Raman peaks of BiOBr were exhibited by BOB-NS, as shown in Fig. 4A. The strong peaks at 59 and $115\, cm^{-1}$ could be assigned to the A_{1g} internal Bi–Br stretching mode, whereas the small peak at $93\, cm^{-1}$ corresponded to A_{1g} first-order vibration modes of Bi metal [17,30]. Meanwhile, the peak at $162\, cm^{-1}$ could be attributed to the E_g Bi–Br stretching mode [31]. All these sharp and intense peaks implied that BOB-NS is of high crystallinity. After visible light irradiation, BOB-NS-VLT demonstrated severe broadening and weakening of peaks, accompanied with peaks shifted to lower frequency. This phenomenon further manifested the presence of OVs, where the displacement of oxygen atoms led to the lattice distortion and crystallinity weakening of BOB-NS-VLT [32]. All these characterization provided undeniable evidences for the successful
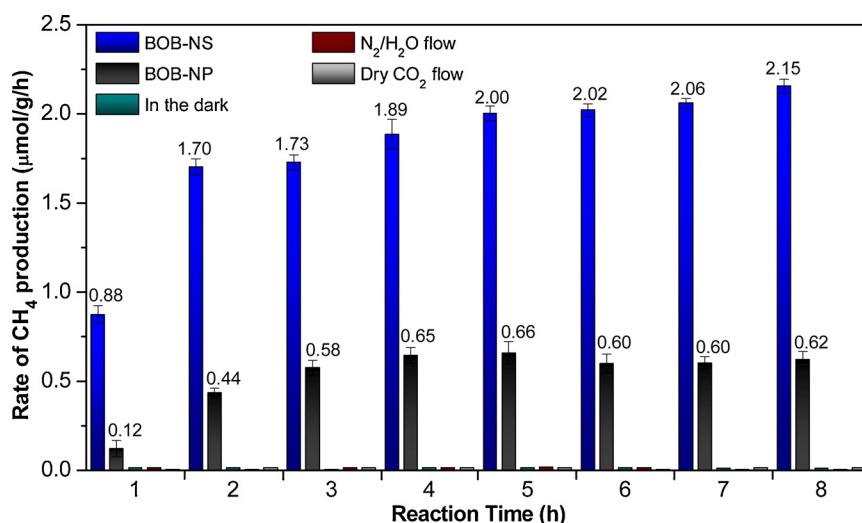
Fig. 2. Time dependence of photocatalytic CH_4 production rate over BOB-NS and BOB-NP under visible light irradiation (λ > 400 nm). Control experiments performed in the absence of light, under N_2/H_2O flow and dry CO_2 flow are also included.

introduction of surface OVs on BOB-NS-VLT, providing prerequisite for studying the pivotal effects of OVs on photocatalytic activities.

To ascertain the presence of OVs for enhanced photocatalytic performance, optical properties of the as-developed samples were examined. As shown in Fig. 4B inset, the BOB-NS before light irradiation appeared to be in yellowish-white colour, whereas a fascinating colour change to blackish-grey was observed on the area with direct light

irradiation. The stark alteration of the colour was reflected by the UV–vis absorption spectra of BOB-NS and BOB-NS-VLT (Fig. 4B). As expected, the presence of OVs on BOB-NS-VLT greatly enhanced the light absorption of the sample in the visible light region, as a result of the occurrence of indirect sub-band excitation which alters the optical properties of the semiconductor. Similar phenomenon of OV-enhanced absorption has also been reported in the literature [33]. Based on the
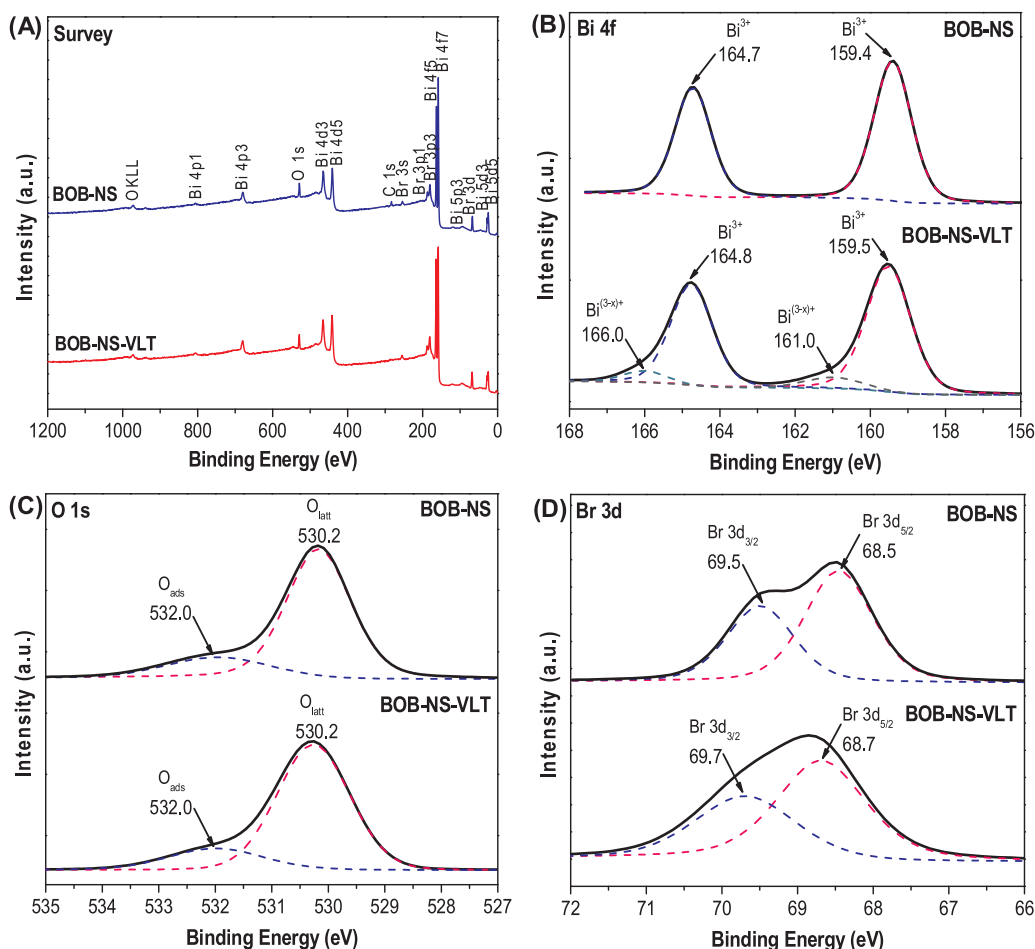

Fig. 3. (A) XPS survey spectra of BOB-NS and BOB-NS-VLT. High resolution (B) Bi 4f, (C) O 1s and (D) Br 3d spectra of BOB-NS and BOB-NS-VLT.
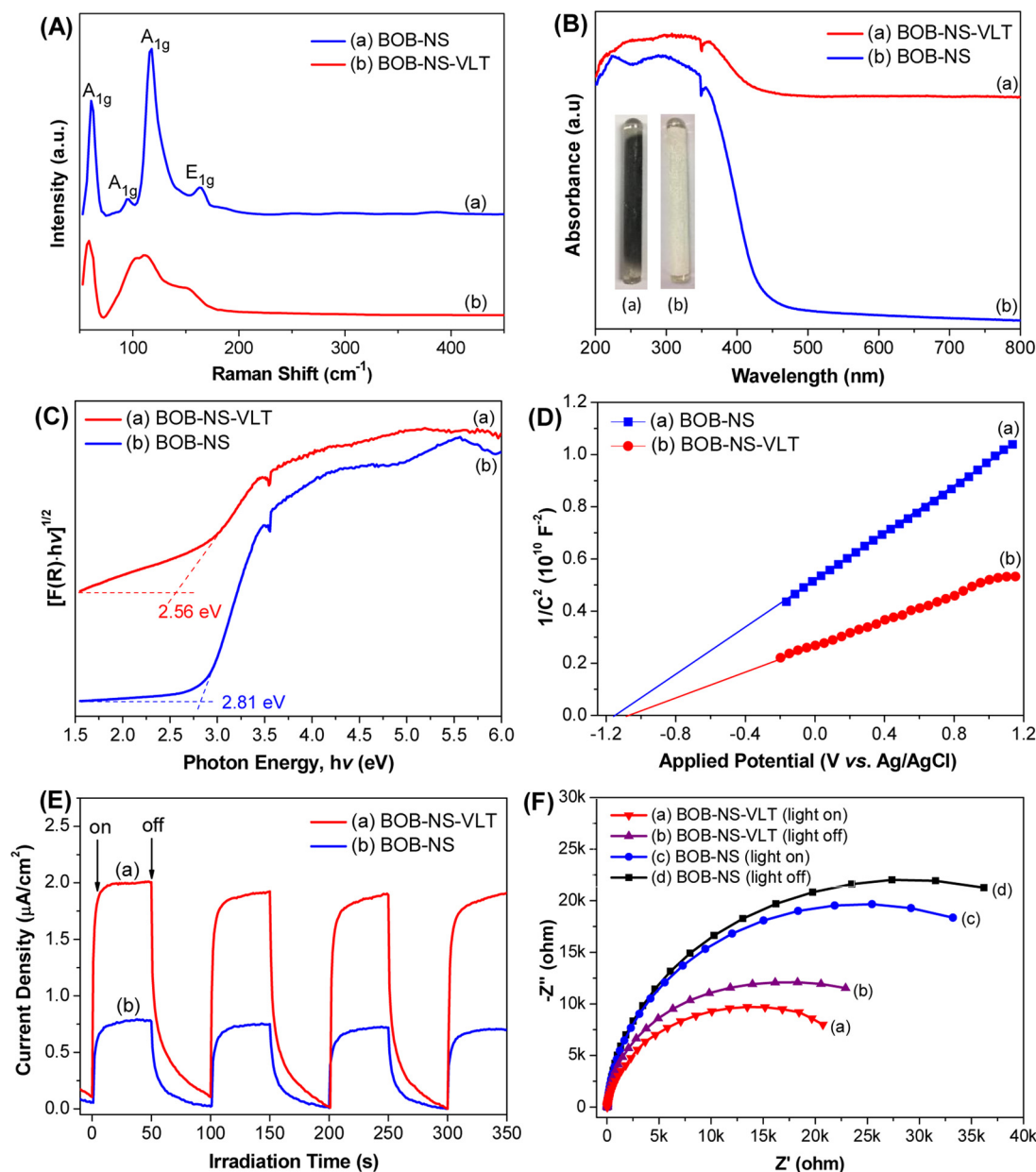
Fig. 4. (A) Raman spectra, (B) UV–vis DRS (insets show the colours of sample before and after visible light irradiation), (C) Tauc plots of modified Kubelka-Munk (*KM*) function, (D) Mott-Schottky plots, (E) Transient photocurrent responses and (F) EIS Nyquist plots of BOB-NS and BOB-NS-VLT.

Tauc plots in Fig. 4C, the bandgap energies of BOB-NS and BOB-NS-VLT were estimated to be 2.81 and 2.56 eV, respectively. This bandgap-narrowing suggested that surface OV engineering is an effective approach to tailor the electronic structures of the semiconductors.

To elucidate this, Mott-Schottky analysis was performed to shed some light on the electronic band potentials of the samples. As shown in Fig. 4D, the flat band potentials (E_{fb}) of BOB-NS and BOB-NS-VLT were found to be −1.15 and −1.06 V *vs.* Ag/AgCl, which are equivalent to −0.95 and −0.86 V *vs.* normal hydrogen electrode (NHE), respectively. Besides, the positive slopes of the Mott-Schottky plots manifested that the samples are of n-type semiconductors [34]. As widely accepted, the CB potentials of n-type semiconductors are 0–0.2 V higher than the E_{fb}, depending on both carrier concentration and electron effective mass [35]. In this case, the difference was set as 0.1 V, hence the CB minimum are −1.05 and −0.96 V for BOB-NS and BOB-NS-VLT, respectively. Working in conjunction with the bandgaps determined from Tauc plots, the VB maximum were estimated to be positioned at 1.76 V for BOB-NS and 1.60 V for BOB-NS-VLT. This phenomenon of OV-

induced bandgap narrowing along with CB edge downshifting and VB edge uplifting was concordant with our previous work [36] and other literature [37,38]. It is worth highlighting that BOB-NS-VLT exhibited a substantially smaller Mott-Schottky slope compared to BOB-NS, indicating that the donor density of BOB-NS-VLT was remarkably increased after the introduction of OV defects [39]. This enhancement in donor density could facilitate the charge separation and transport, resulting in an improved charge collection efficiency and retarding the recombination of charge carriers, which were corroborated by the transient photocurrent responses of the samples.

Transient photocurrent response measurement with onset potential under intermittent light irradiation is a direct reflection of the charge transfer behaviours, for instance, the lifetime of photogenerated charge carriers and the efficiency of electron-hole pairs separation [40]. As disclosed in Fig. 4E, BOB-NS-VLT displayed a stark improvement of photocurrent density than BOB-NS under similar applied potential of 0.1 V *vs.* Ag/AgCl. It is strongly entrenched that the inlaid of surface OVs on BiOBr could promote efficient electron-hole pairs isolation and
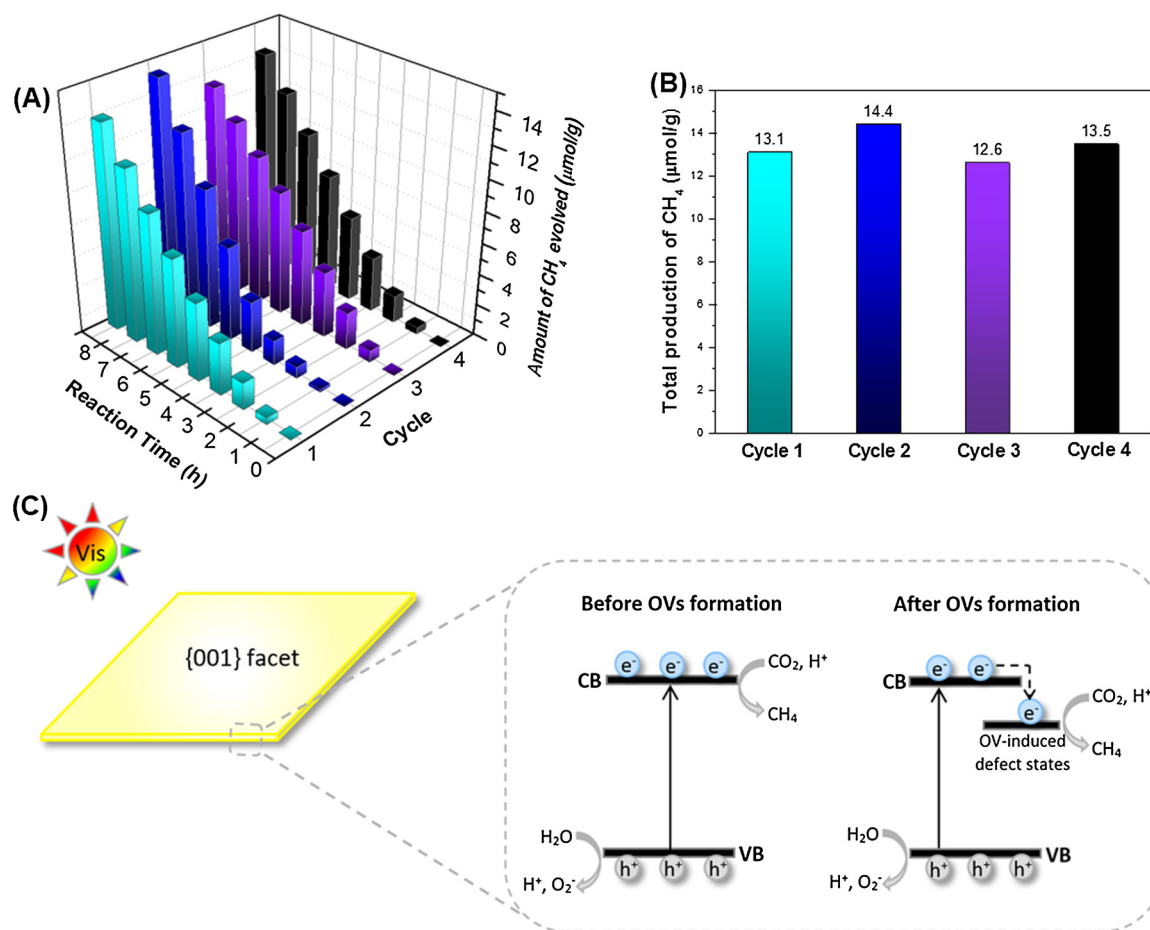
Fig. 5. Photostability tests of BOB-NS for repeated photocatalytic CO_2 reduction under visible light irradiation: (A) time courses of CH_4 evolution, (B) accumulated evolution of CH_4 from each test cycle and (C) Schematic illustration of the mechanisms of CO_2 photoreduction into CH_4 over BOB-NS before and after OVs formation.

prolong the lifetime of photogenerated charge carriers. The formation of higher photocurrent responses of BOB-NS-VLT was attributed to the rapid diffusion of excitons to the back contact which indicates its lower charge recombination as compared to its forebear BOB-NS. To further elucidate the transfer properties of the photogenerated charge carriers, the samples were examined by electrochemical impedance spectroscopy (EIS) Nyquist plots. Fig. 4F shows a smaller arc radius of BOB-NS-VLT as compared to BOB-NS under both dark condition and visible light irradiation. The depressed semicircle of BOB-NS-VLT reflects its facilitated charge transfer ability with lower interfacial layer resistance. This indicates that the presence of surface OVs could accelerate the charge shuttle and exemplify a facile electron relaying process. These findings elucidated the indispensable roles of OVs played for remarkable photocatalytic activities, which would be corroborated through the stability tests of the as-fabricated photocatalyst.

As demonstrated in Fig. 5A and B, BOB-NS exhibited superior performance over four consecutive test cycles under identical experimental conditions. These findings suggested that the as-prepared photocatalyst possesses excellent recyclability and long-term stability for repeated applications. It is worth noting that the second test cycle produced higher amount of CH_4 than first cycle, which could be accredited to the sufficient irradiation time for the generation of abundant surface OVs on BOB-NS. As divulged by the transient photocurrent responses and EIS Nyquist plots, the existence of OVs is beneficial for the transfer and separation of photogenerated charge carries, thereby hindering the recombination of electron-hole pairs and enhancing its photocatalytic performance. In addition, the optical properties of the sample were significantly altered after the generation of OVs (reflected by UV–vis absorption spectra), which guaranteed more light absorption to initiate

the generation of electron hole pairs. As manifested in our previous works, the OV sites not only effectively trap the photoinduced electrons, it could also act as the adsorption sites for CO_2 molecules, where the CO_2 molecules were spontaneously activated to $\cdot CO_2^-$ radicals through accepting electrons from the OV sites [36,41]. In the context of CO_2 photoreduction, this is highly desirable as the formation of $\cdot CO_2^-$ radicals is the rate determining step of the reaction. Furthermore, the attractions between CO_2 molecules and OV sites would generate unexpected infinity interactions, which could lower the energy barriers for interfacial charge transfers. Generally, free O atoms from the dissociation of CO_2 would reoxidize the sample surface, leading to the termination of photocatalytic reactions [29,42]. However, in this case, the visible light-induced OVs formation could maintain the performance of the BOB-NS, as these OVs were *in situ* refreshed as the reaction proceeded. This was evidenced by the long-term stability of these samples, where insignificant deterioration of the activity was observed after four repeating cycles.

Since the existence of surface OVs rendered effective charge separation and inhibited electron-hole pairs recombination through the trapping of electrons at the OV-induced defect states, the mechanisms of photocatalytic CO_2 reduction over BOB-NS before and after the formation of OVs were proposed and illustrated in Fig. 5C. Considering the highly facile preparation of ultrathin BOB-NS and its superior and long-lasting photocatalytic activities, it is believed that BOB-NS would be a promising next generation photocatalyst for a myriad of applications.

4. Conclusions

In summary, ultrathin BiOBr nanosheets with primarily exposed

{001} facets were successfully synthesized through a highly facile one-step hydrothermal approach. The high exposure of {001} facets induced easy formation of surface OVs, where these OV defects were clearly detected on the sample after visible light irradiation. The concomitant effects of the surface OV defects, dominantly exposed highly active {001} facets and ultrathin nanostructures of BOB-NS led to its superior performance in photocatalytic CO_2 reduction. Notably, BOB-NS exhibited a highest CH_4 production yield of $2.15\,\mu mol\,g^{-1}\,h^{-1}$, demonstrating a 3.3^- fold improvement over its pristine BiOBr nanoplates counterpart (BOB-NP) under visible light illumination. In comparison to other photocatalysts which require post-treatments or strong reducing agents to regenerate the OVs, the OV defects on BOB-NS could be easily formed and refreshed during the visible-light-driven CO_2 photoreduction, leading to sustainable active sites for long-term photoactivities. We believe that the findings from the current study would deliver some in-depth and imperative insights that the spatial location engineering of OVs could be an efficient and cost-effective approach for designing photocatalysts with remarkable performance.

Acknowledgements

Appendix A. Supplementary data

Supplementary material related to this article can be found, in the online version, at doi:https://doi.org/10.1016/j.cattod.2018.04.018.

References

[1] W. Tu, Y. Zhou, Z. Zou, Adv. Mater. 26 (2014) 4607–4626.
[2] K. Li, B. Peng, T. Peng, ACS Catal. 6 (2016) 7485–7527.
[3] S. Xie, Q. Zhang, G. Liu, Y. Wang, Chem. Commun. 52 (2016) 35–59.
[4] L. Li, Hao Li, Jie Ai, Zhihui Jia, Falong Zhang, Angew. Chem.- Int. Ed. (2017), http://dx.doi.org/10.1002/ange.201705628.
[5] H. Hirakawa, M. Hashimoto, Y. Shiraishi, T. Hirai, J. Am. Chem. Soc. 139 (2017).
[6] Y. Pan, Z. Sun, H. Cong, Y. Men, S. Xin, J. Song, S.-H. Yu, Nano Res. 9 (2016) 1689–1700.
[7] Y. Liu, B. Wei, L. Xu, H. Gao, M. Zhang, ChemCatChem 7 (2015) 4076–4084.
[8] J.L. White, M.F. Baruch, J.E. Pander III, Y. Hu, I.C. Fortmeyer, J.E. Park, T. Zhang, K. Liao, J. Gu, Y. Yan, T.W. Shaw, E. Abelev, A.B. Bocarsly, Chem. Rev. 115 (2015) 12888–12935.
[9] L. Liu, C. Zhao, Y. Li, J. Phys. Chem. C 116 (2012) 7904–7912.
[10] C. Yang, B.C. Wood, V.R. Bhethanabotla, B. Joseph, J. Phys. Chem. C 118 (2014) 26236–26248.
[11] V.P. Indrakanti, H.H. Schobert, J.D. Kubicki, Energy Fuels 23 (2009) 5247–5256.
[12] H. Li, J. Shang, Z. Ai, L. Zhang, J. Am. Chem. Soc. 137 (2015) 6393–6399.
[13] J. Li, Y. Yu, L. Zhang, Nanoscale 6 (2014) 8473–8488.
[14] Z. Yang, J. Li, F. Cheng, Z. Chen, X. Dong, J. Alloys Compd. 634 (2015) 215–222.
[15] J. Li, K. Zhao, Y. Yu, L. Zhang, Adv. Funct. Mater. 25 (2015) 2189–2201.
[16] L. Ye, Y. Su, X. Jin, H. Xie, C. Zhang, Environ. Sci. Nano 1 (2014) 90–112.
[17] D. Wu, B. Wang, W. Wang, T. An, G. Li, T.W. Ng, H.Y. Yip, C. Xiong, H.K. Lee, P.-K. Wong, J. Mater. Chem. A 3 (2015) 15148–15155.
[18] L. Li, L. Ai, C. Zhang, J. Jiang, Nanoscale 6 (2014) 4627–4634.
[19] H.F. Cheng, B.B. Huang, Y. Dai, Nanoscale 6 (2014) 2009–2026.
[20] H. Xing, H. Ma, Y. Fu, X. Zhang, X. Dong, X. Zhang, J. Renew. Sustain. Energy 7 (2015) 063120.
[21] Y. Lv, W. Yao, R. Zong, Y. Zhu, Sci. Rep. 6 (2016) 19347–19356.
[22] L. Ye, L. Zan, L. Tian, T. Peng, J. Zhang, Chem. Commun. 47 (2011) 6951–6953.
[23] H.G. Yang, C.H. Sun, S.Z. Qiao, J. Zou, G. Liu, S.C. Smith, H.M. Cheng, G.Q. Lu, Nature. 453 (2008) 638–641.
[24] D.Z.L.W. Tian, Zhi-You Na, Zhou Shi-Gang, Sun Yong, Science 316 (2007) 732–735.
[25] X.Y. Kong, W.L. Tan, B.-J. Ng, S.-P. Chai, A.R. Mohamed, Nano Res. 10 (2017) 1720–1731.
[26] X. Pan, M.-Q. Yang, X. Fu, N. Zhang, Y.-J. Xu, Nanoscale 5 (2013) 3601–3614.
[27] H. Li, J. Shi, K. Zhao, L. Zhang, Nanoscale 6 (2014) 14168–14173.
[28] H. Li, T. Hu, J. Liu, S. Song, N. Du, R. Zhang, W. Hou, Appl. Catal. B Environ. 182 (2016) 431–438.
[29] L. Zhang, W. Wang, D. Jiang, E. Gao, S. Sun, Nano Res. 8 (2015) 821–831.
[30] K. Zhang, J. Liang, S. Wang, J. Liu, K. Ren, X. Zheng, H. Luo, Y. Peng, X. Zou, X. Bo, J. Li, X. Yu, Cryst. Growth Des. 12 (2012) 793–803.
[31] J. Wang, Y. Zhang, L. Tian, F. Liu, Q. Xia, J. Nanoparticle Res. 16 (2014) 2691–2699.
[32] Y. Yu, C. Cao, H. Liu, P. Li, F. Wei, Y. Jiang, W. Song, J. Mater. Chem. A 2 (2014) 1677–1681.
[33] S. Wang, X. Hai, X. Ding, K. Chang, Y. Xiang, X. Meng, Adv. Mater. 29 (2017) 1701774–1701780.
[34] X. Wu, Y.H. Ng, L. Wang, Y. Du, S.X. Dou, R. Amal, J. Scott, J. Mater. Chem. A 5 (2017) 8117–8124.
[35] X. Tu, S. Qian, L. Chen, L. Qu, J. Mater. Sci. 50 (2015) 4312–4323.
[36] X.Y. Kong, Y.Y. Choo, S.-P. Chai, A.K. Soh, A.R. Mohamed, Chem. Commun. 52 (2016) 14242–14245.
[37] W. Bi, C. Ye, C. Xiao, W. Tong, X. Zhang, W. Shao, Y. Xie, Small 10 (2014) 2820–2825.
[38] G. Zhang, Z. Hu, M. Sun, Y. Liu, L. Liu, H. Liu, C.-P. Huang, J. Qu, J. Li, Adv. Funct. Mater. 25 (2015) 3726–3734.
[39] T. Su, Y. Yang, Y. Na, R. Fan, L. Li, L. Wei, B. Yang, W. Cao, ACS Appl. Mater. Interfaces 7 (2015) 3754–3763.
[40] B.-J. Ng, L.P. Kurnianditia, X.Y. Kong, K.P.Y. Shak, P. Pasbakhsh, S.-P. Chai, A.R. Mohamed, Appl. Catal. B Environ. 224 (2018) 360–367.
[41] X.Y. Kong, W.P.C. Lee, W.-J. Ong, S.-P. Chai, A.R. Mohamed, ChemCatChem 8 (2016) 3074–3081.
[42] M. Nolan, S.C. Parker, G.W. Watson, Surf. Sci. 595 (2005) 223–232.